Structure and flexural properties of 3D needled carbon fiber reinforced carbon and silicon carbide (C/C-SiC) composites fabricated by gaseous and liquid silicon infiltration

Short title: Structure and flexural properties of GSI/LSI 3D needled C/C-SiC Composites

Fan Wan[1], Talha.J Pizada[2], Rongjun Liu*[1], Yanfei Wang[1], Gongjin Qi[3], Changrui Zhang[1] and Thomas James Marrow*[2]

1. College of Aerospace Science and Technology, National University of Defense Technology, Changsha, 410073, China
2. Department of Materials, University of Oxford, Oxford, OX1 3PH, UK
3. Aeronautical Technology Research Center, Beijing, 100076, China

*Corresponding Author:

Thomas James Marrow, james.marrow@materials.ox.ac.uk
Tel: 01865 273938, Fax: 01865 273289,
Email: james.marrow@materials.ox.ac.uk

Rongjun Liu, rongjunliu@nudt.edu.cn

Tel: +86 13755168115
Email: rongjunliu@nudt.edu.cn

Abstract

3D needled carbon fiber reinforced composites (C/C-SiC) were fabricated by gaseous silicon infiltration (GSI) for different reaction times, followed by further densification with liquid silicon infiltration (LSI). The density, flexural modulus and flexural strength increased as a spatially connected SiC structure developed, but the flexural strength could be degraded by a long total reaction time. The composites all exhibited quasi-brittle fracture with fiber bundle pull-out and interfacial debonding. Fracture could propagate within the needle bundles that were perpendicular to the tensile stress.

Key Words

C/C-SiC; Gaseous Silicon Infiltration; Liquid Silicon Infiltration; Densification; Flexural properties; X-ray Computed Tomography; Mercury Intrusion Porosimetry

1 Introduction

Because of their superior mechanical, physical and chemical properties, carbon fiber reinforced carbon and silicon carbide composites (C/C-SiC) has been proposed as materials for aerospace structural [1], advanced friction [2] and space mirror systems [3], and also for advanced nuclear energy [4] and ballistic protection [5]. There are three frequently used preparation methods for C/C-SiC composites: Chemical Vapor Infiltration (CVI), Precursor Infiltration and Pyrolysis (PIP) and Silicon Infiltration (SI) [6–9]. The SI methods include Liquid Silicon Infiltration (LSI) [10] and Gaseous Silicon Infiltration (GSI) [11]. They require a much shorter fabrication period than CVI and PIP, and so SI has been proposed as an effective way to produce low-cost C/C-SiC composites. In the LSI process, the liquid Si reacts with the carbon matrix, so it is also known as the Reactive Melt Infiltration (RMI) method. Studies related to LSI have mainly involved infiltration modelling, reaction kinetics, and the roles of fiber coating and melt composition on material properties [1,12–14]. There have been fewer studies carried out on GSI, in which Si infiltrates into sample in gaseous form. GSI is a relatively more gentle reaction process than LSI and might be beneficial to the mechanical properties [9,15]. Previous studies of C/C-SiC composites produced by GSI have shown that microstructure defects and porosity have a significant effect on mechanical properties [16,17]. However, the details of the GSI process and the reaction mechanism, and their effects on densification and the spatial distributions of material and pores, require further study.

In this study, 3 dimensional (3D) needled C/C-SiC composites were fabricated by the GSI method, with LSI applied for further densification. Different GSI fabrication times were used to study the densification process. The flexural modulus and strength of the composites were evaluated by three-point bending. The microstructural features, including phase composition and pore morphology, were analyzed by Scanning Electron Microscopy (SEM) with Energy Dispersive Spectroscopy (EDS), X-ray Diffraction (XRD), X-ray Tomography (XCT) and Mercury Intrusion Porosimetry (MIP). The

aim of this work was to explore in detail the structural evolution during the GSI process, in order to support the design of the low-cost and high-performance C/C-SiC composites.

2 Experimental

2.1 Material

3D needled C/C preforms with a fiber volume fraction of ~30% (T300 carbon fiber, 7 μm diameter) were prepared through Chemical Vapor Infiltration (CVI) by the Composites Institute of Tianjing Technology University (China). The schematic of the 3D needled structure of the preform in Fig. 1a shows the non-woven fiber cloths (0°/90° orientation), the short-cut web of randomly oriented fibers, and the needle fibers that stitch the cloth layers together. In the CVI process, propylene and argon were used as precursor and carrier diluting gases respectively and the reaction was carried out at 960°C. After CVI, the C/C preform (Fig. 1b) had a density of 1.28 g/cm^3 with a thickness of 1 ~ 1.5 μm of PyC in the cloth region (Fig. 1c) and 4 ~ 5 μm in the web region (Fig. 1d). C/C-SiC composites were fabricated from the C/C preform by GSI, with reaction times of 0.5 h, 1.0 h, 1.5 h and 2.0 h at 1700°C. Samples of these were further densified by LSI at 1700°C for 2 h. The test specimens were cut by wire cutting electrical discharge machining (WEDM) at the National University of Defense Technology, China.

2.2 Characterization

The sample densities were measured by the Archimedes principle and their phase compositions and total porosities were obtained by gravimetric analysis [18] using sample sizes of 5 mm × 5 mm × 10 mm and 4 mm × 2 mm × 10 mm, respectively. SEM (HITACHI S-4800, Japan, with EDS) was employed to observe the microstructure morphology, and the phase compositions were investigated by XRD (D8 Advance, Bruker/Axs Corp., Germany). The open pores were characterised by MIP at Nanjing Forestry University, using an AutoPore IV9510 Hg-porosimeter (Micromeritics).

An Xradia Versa 510 X-ray microscope (University of Oxford), operated at 80 keV energy and 7 W power was used for 3D characterization of the microstructures, in cuboid samples with dimensions of less than 5 mm in each dimension. 1600 projections were recorded through 360° for each scan, which required about 2 hours and 30 minutes (x2 binning, reconstructed volume as a cylinder of ~1000 voxel radius x 1000 voxels high, with a voxel size of 6 μm). The instrument software and Avizo 9.3.0 were used for tomograph reconstruction and visualization.

Three-point bending tests were conducted on samples with dimensions of 75 mm (cloth direction) × 10 mm (cloth direction) × 4 mm (needle direction), with 5 samples tested for each material. The tests were performed in a 1 kN capacity WDW-100KN universal testing machine (Changchun Research Institute of Testing Machines, Jilin, China), at a crosshead displacement speed of 0.5 mm/min and a loading span of 64 mm.

3 Results

3.1 Microstructure Characterization

The density and phase compositions of the composites after GSI are reported in Table 1. The density increased by 0.8% to 62.5%, relative to the initial density of the C/C preform, with increasing reaction time from 0.5 h to 2.0 h. The volume fractions of C and the open porosity decreased, while the volume fractions of SiC and Si increased. The densities and phase compositions of the C/C-SiC composites after the LSI process (Table 2) are similar to each other, with no dependency on GSI process time. The XRD analysis (Fig. 2) confirms the trends of general decreasing C and increasing SiC and Si with increasing GSI reaction time, as shown qualitatively by peak height. In the composites that were further reacted by the LSI process, the proportions of C, SiC and Si indicated by XRD are also relatively constant with no clear effect of the initial GSI process time.

The SEM images of cross-sections (Fig. 3) show increasing densification of the matrix with GSI reaction time. The shortest reaction time (0.5 h) deposited some matrix onto the surface of fibers. This increased at 1.0 h and formed a massive structure in most regions at 1.5 h. The composite is visibly most dense at 2.0 h, other than some large pores. Higher resolution SEM images of the same composites (Fig. 4) confirm that the matrix deposited uniformly on fibers at 0.5 h (Fig. 4a), with a thickness of ~ 0.5 μm estimated by backscatter electron microscopy (Fig. 4e). As the process time increases to 1.0 hr, the fibers tend to join (Fig. 4b) as the deposited matrix thickens to 2 ~ 3 μm (Fig. 4f). At 1.5 h and 2.0 h, the matrix tends to close the smaller pores (Fig. 4c and Fig. 4d), as its thickness, estimated from observations within large pores, reaches ~10 μm to 20 μm (Fig. 4g and h). The additional reaction by 2.0 h LSI produced a dense structure with few large pores in all composites (Fig.5).

EDS analysis was used to further investigate the elemental and phase distributions. In the composite fabricated with 0.5 h of GSI, Si can be detected at least 2 μm from the fiber centre (Fig.6a). In the matrix, for example at 1.5 h (Fig. 6b), the ratio of Si to C is typically close to 1:1 (e.g. point 1) indicating it is predominantly SiC, but other regions of matrix (e.g. point 2) have high residual Si, which is supported also by the observation of white regions (i.e. Si, which gives some backscattered electron contrast). After 2.0 h of GSI, there is a significant amount of Si (Fig. 6c) in the matrix and it also deeply penetrates the fibers.

To observe the morphology of the phases, composites were etched in a mixture of nitric and hydrofluoric acids at 40°C to dissolve the residual Si (this is the first step of gravimetric analysis). SEM examination confirms that after 0.5 h GSI, SiC had formed on the surface of fibers as a thin layer (Fig. 7a, e), while after 1.0 h GSI SiC grains with a size of less than 5 μm were forming on the fiber surface (Fig. 7b, f). These increased in size with increasing GSI process time (Fig. 7c, g) and reached ~30 μm at 2.0 h (Fig. 7d, h). The SiC grains has irregular polyhedral shapes, although in the composite

with 2.0 h GSI some SiC grains were elongated and had a size of more than 50 μm (Fig.7h). After the LSI process, SiC grains were observed with sizes from several μm to ~50 μm for both the initial 0.5 h and 1.0 h GSI initial processing (Fig. 7i, j), with more massive SiC developed in the composites that had 1.5 h and 2.0 h GSI initial processing (Fig. 7k, l).

XCT was also used to examine the composites that has been etched to remove residual Si. The different X-ray attenuation of C and SiC allows their segmentation and labelling, and 3D visualizations of the SiC distributions for the 1.0 h GSI, 2.0 h GSI and 1.0 h GSI + 2.0 h LSI samples are shown in Fig. 8. These have labeled volume fractions are 17.3%, 26.3% and 32.2% respectively. The SiC in the 1.0 h GSI sample is present as discrete blocks of different size (Fig. 8a), while at 2.0 h GSI the SiC has developed into a connected structure (Fig. 8b). The SiC structure is most solid and spatially connected after 1.0 h GSI + 2.0 h LSI (Fig. 8c).

The porosity was also characterised by image segmentation in tomographs of un-eteched samples (Fig.9), and the labeled porosity content was 18.6% at 1.0 h GSI, 5,5% at 2.0 h GSI and 2.3 % at 1.0 h GSI + 2.0 h. The porosity is mostly connected at 1.0 h GSI, has much lower connectivity at 2.0 h GSI (regions that are unconnected at the image resolution are shown with different colors), and is quite isolated at 1.0 h GSI + 2.0 h LSI in which high aspect ratio intra-bundle pores and low aspect ratio round gas pores are observed.

The MIP characterization of the open porosity in the un-etched samples is summarised in Fig.10 and also Tables 1 and 2. The measured pore diameter range is similar in all samples, ranging a few tenths of μm to several hundred of μm. The largest pore volume in the GSI-only samples is mostly within the range of 20 to 30 μm, and it decreases significantly with increasing reation time. The GSI+LSI samples all have low volumes of open porosity that are quite uniformly distributed over the pore diameter range, with the highest porosity for 0.5 h GSI + 2 h LSI.

3.2 Flexural Properties

Typical load-displacement curves obtained in three-point bending show quasi-brittle failure in all samples (Fig.11). The flexural strengths and elastic moduli are summarised in Table 3. The flexural strength was calculated at the peak load, and the modulus was assessed from the linear region up to 60% of the peak load. The strength and modulus increase with GSI process time from 117±18 MPa and 14±3 GPa at 0.5 h to 185±17 MPa and 26±6 GPa at 2.0 h. The flexural strength of the GSI+LSI samples tends to decrease with increasing GSI process time, from 203±8 MPa at 0.5 h GSI+ 2.0 h LSI to 146±16 MPa at 2.0 h GSI + 2.0 h LSI. The flexural modulus after LSI is relatively constant, at 27±2 GPa at 0.5 h GSI + 2.0 h LSI and 28±4 at 2.0 h GSI + 2.0 h LSI. Slightly higher moduli of 32±3 GPa are observed at the intermediate GSI times. SEM fractography (Fig.12) demonstrates that all tested samples have significant fiber bundle and fiber pull-out and interfacial debonding. Qualitatively, there appears to be a trend of increasing fiber pull-out length with increasing reaction time in the GSI samples (Fig. 12a), with less pull-out in the GSI+LSI samples (Fig. 12b).

XCT characterization of the 1.0 h GSI and 2.0 h GSI processed samples, performed after the bending tests, was used to investigate their internal damage. Unloaded specimens were scanned that had been tested to the maximum displacement (i.e. Fig. 11). The volume examined in each was centered at the location of maximum bending moment. In the 1.0 h GSI sample (Fig. 13a), fracture of the non-woven fiber bundles can be observed. The pattern of damage in the 2.0 h GSI sample is similar and interfacial cracks can also be observed (Fig. 13b). Cracking was able to propagate within the needle-stitched regions in both examples; this is illustrated in the 3D visualization of the dominant cracks in the 2.0 h GSI (Fig. 13c), where the convoluted crack path is associated with the needle-stitch.

Discussion

The observations of C/C-SiC composites fabricated by the GSI method show two morphologies of SiC. These are layered SiC, which grows from the C interface, and granular SiC. For example, the SiC layer has a thickness less than 5 μm (Fig. 7b) after 1.0 h of GSI, and at this stage granular SiC has already formed. The same structures have been observed in C/C-SiC composites fabricated by the LSI method [19]. Characterising the distribution of residual Si and SiC in silicon infiltrated composites is difficult using conventional ceramographic analyses such as backscatter electron microscopy, but by combining non-destructive XCT with gravimetric analysis, the 3D structures of the SiC distibution that develops during GSI have been observed (Fig. 8). After 2.0 h GSI, the SiC forms a spatially connected structure (Fig. 8b) that is accompanied by improved mechanical properties. The matrix distribution, which also affects the propagation of cracking (Fig. 13). is affected by the arrangement of the carbon fibers. The observations are consistent with a previoius study of a similarly GSI-produced needle-stitched C-C/SiC composite that showed many randomly arranged short-cut fibers within the SiC, while in the cloth region the SiC was found only in the pores between the fiber bundles that were introduced by the needle insertion [17].

There are three widely-accepted mechanisms of the C-Si reaction in the LSI process: dissolution-precipitation [12,20]; diffusion-control [21,22] and interface-control [23]. In the GSI process, there is no liquid Si and thus no dissolution of C can occur. From the observations in Fig. 3 to Fig. 7, the C-Si reaction process in GSI can be divided into two stages. In stage I, gaseous Si is absorbed at the fiber surface and reacts with the CVI-deposited PyC. Interdiffusion of Si and C then occurs (Fig. 6a), and as the surface of PyC is rough (Fig. 1d) the surface of the formed SiC is also rough. In stage II, layered SiC has formed and the reaction is then controlled by the diffusion of Si and C through the layered SiC, similar to the LSI process. After stage II, any redundant Si remains un-reacted as residual Si.

The GSI process is limited by transport of gaseous Si, so the rate of densification decreases with increasing time as the open porosity reduces; a significant density change was observed from 0.5 h to 1.0 h that then slowed with increasing process time (Table 1). In the 3D needled C/C preform structure (Fig. 1), the web region contains larger pores, which are more readily infiltrated by gaseous Si and also have a much thicker PyC layer for the same reason. Both factors will encourage the C-Si reaction, so the matrix primarily formed in this region in all the composites (Fig.3 and Fig.5). Before SI processing, there are also inter-fiber pores within the fiber bundles of the cloth (i.e. intra-bundle pores) (Fig. 1) that have dimensions close to the fiber diameter (~7 μm). After the GSI and GSI+LSI processing, there are more and larger intra-bundle pores (Fig. 3 and Fig. 5), with some existing as intra-bundle cracks (Fig. 3f and Fig. 5c). These arise from the mismatch of thermal expansion of the fibers and matrix on cooling from the high temperature SI process [17], and the MIP analysis (Fig. 10) shows they form the greatest part of the open poroity.

The effect of the LSI densification process, applied after GSI, is most significant for the 0.5 h and 1.0 h GSI composites. The strengths and flexural moduli increased because of the denser structures, and the SiC layer formed in the GSI process is also expected to have protected the fibers from Si erosion in the LSI process. The 1.5 h GSI and 2.0 h GSI were less affected as the space for further densification is limited. The modulus increased with denstiy, but the lower strength of the 2.0 h GSI + LSI composite, compared with 2.0 h GSI, may be due to some fiber damage from the long reaction time and also coarsening of the SiC grains (Fig.7).

Comparison of the total porosity and open porosity (Table 1 and Table 2) shows an increasing proportion of closed porosity with longer GSI reaction time. The closed pores are mostly inter-bundle pores in the web region (Fig. 3 and Fig. 5). These pores may affect the crack propagation path, but the observations of the flexural failure of the composites of 1.0 h and 2.0 h GSI show that failure of the cloth fiber bundles is quite important (Fig. 13). Needle bundles have been shown to provide beneficial

lateral restraint to resist fracture between the cloth layers in compressive loading parallel to the cloth direction [17], but they can introduce a weak path for cracks to propagate when tension is applied parallel to the cloth layers in flexural loading (Fig. 13).

4 Conclusion

3D needled C/C-SiC composites have been fabricated by GSI and LSI to investigate the effects of the GSI process time on structure and properties. As the GSI process time increased, from 0.5 h to 2.0 h, there was a progressive increase in density and flexural properties. LSI for 2.0 h caused further densification, particularly with lower initial density, but degraded the strength at higher initial density. The SiC distribution was affected by the original porosity, and a more connected structure developed with increasing reaction time. The stitched needles, which were perpendicular to the applied tensile stress in flexural loading, had lower resistance to fracture.

5 Acknowledgements

We acknowledge EPSRC Grant EP/M02833X/1 “University of Oxford: experimental equipment upgrade” for supporting the Xradia Versa 510 microscope and facilities for 3D data analysis and visualization. The research is part of the Project 2018JJ1029 supported by Hunan Provincial Natural Science Foundation of China.

6 References

[1] M. Patel, K. Saurabh, V.B. Prasad, J. Subrahmanyam, High temperature C/C-SiC composite by liquid silicon infiltration: A literature review, Bulletin of Materials Science. 35 (2012) 67–77. doi:10.1007/s12034-011-0247-5.

[2] Z. Li, P. Xiao, B. gu Zhang, Y. Li, Y. hai Lu, Preparation and tribological properties of C/C-SiC brake composites modified by in situ grown carbon nanofibers, Ceramics International. 41 (2015) 11733–11740. doi:10.1016/j.ceramint.2015.05.139.

[3] L.. Huang, L. R.J, C.. Zhang, Y.. Wang, Y.. Cao, Si/SiC optical coatings for C/SiC composites via gel-casting and gas silicon infiltration: Effects of carbon black content, Journal of Alloys and Compounds. 711 (2017) 162–168. doi:10.1016/j.jallcom.2017.03.222.

[4] C. Shih, Y. Katoh, L.L. Snead, J. Steinbeck, The effect of neutron irradiation on the mechanical properties of C / SiC composites, Journal of Nuclear Materials. 439 (2013) 192–201. doi:10.1016/j.jnucmat.2013.03.089.

[5] T. Li, Y. Yang, X. Yu, H. Liu, Y. Li, Micro-structure response and fracture mechanisms of C/SiC composites subjected to low-velocity ballistic penetration, Ceramics International. 43 (2017) 6910–6918. doi:10.1016/j.ceramint.2017.02.113.

[6] J. Wang, X. Chen, K. Guan, L. Cheng, L. Zhang, Y. Liu, Effects of channel modification on microstructure and mechanical properties of C/SiC composites prepared by LA-CVI process, Ceramics International. 44 (2018) 16414–16420. doi:10.1016/j.ceramint.2018.06.052.

[7] H. Wang, D. Zhu, F. Wan, W. Zhou, F. Luo, Influence of the C/C preform density on tribological characteristics of C/C-SiC composites under different conditions, Ceramics International. 40 (2014) 16641–16646. doi:10.1016/j.ceramint.2014.08.025.

[8] J. Si-Zhou, X. Xiang, C. Zhao-Ke, X. Peng, H. Bai-Yun, Influence factors of C/C-SiC dual matrix composites prepared by reactive melt infiltration, Materials and Design. 30 (2009) 3738–3742. doi:10.1016/j.matdes.2009.02.013.

[9] Q. Zhou, S. Dong, X. Zhang, Y. Ding, D. Jiang, Fabrication of Cf/SiC composites by vapor silicon infiltration, Journal of the American Ceramic Society. 89 (2006) 2338–2340. doi:10.1111/j.1551-2916.2006.01018.X.

[10] P. Xiao, Z. Li, X. Xiong, Microstructure and tribological properties of 3D needle-punched C/C–SiC brake composites, Solid State Sciences. 12 (2010) 617–623. doi:https://doi.org/10.1016/j.solidstatesciences.2010.01.014.

[11] H. Wang, X. Zhou, J. Yu, Y. Cao, R. Liu, Fabrication of SiCf/SiC composites by chemical vapor infiltration and vapor silicon infiltration, Materials Letters. 64 (2010) 1691–1693. doi:10.1016/j.matlet.2010.05.013.

[12] R. Pampuch, J. Bialoskbrski, Reaction Mechanism in Carbon-Liquid Silicon Systems at Elevated Temperatures, Ceramics International. 12 (1986) 99–106.

[13] X. Yang, Z. Su, Q. Huang, X. Fang, L. Chai, Microstructure and mechanical properties of C/C-ZrC-SiC composites fabricated by reactive melt infiltration with Zr, Si mixed powders, Journal of Materials Science and Technology. 29 (2013) 702–710. doi:10.1016/j.jmst.2013.05.005.

[14] C. Liu, L. Cao, J. Chen, L. Xue, X. Tang, Q. Huang, Microstructure and ablation behavior of SiC coated C/C-SiC-ZrC composites prepared by a hybrid infiltration process, Carbon. 65 (2013) 196–205. doi:10.1016/j.carbon.2013.08.014.

[15] Q. Zhou, S. Dong, Y. Ding, Z. Wang, Z. Huang, D. Jiang, Three-dimensional carbon fiber-reinforced silicon carbide matrix composites by vapor silicon infiltration, Ceramics International. 35 (2009) 2161–2169. doi:10.1016/j.ceramint.2008.11.023.

[16] F. Wan, S. Zhao, R. Liu, C. Zhang, T.J. Marrow, In situ Observation of Compression Damage in a Three-Dimensional Braided Carbon Fiber Reinforced Carbon and Silicon Carbide (C/C-SiC) Ceramic Composite, Microscopy and Microanalysis. 24 (2018) 227–237. doi:10.1017/S1431927618000351.

[17] F. Wan, R. Liu, Y. Wang, Y. Cao, C. Zhang, T. James, In situ observation of compression damage in a 3D needled-punched carbon fiber-silicon carbide ceramic matrix composite, Composite Structures. 210 (2019) 189–201. doi:10.1016/j.compstruct.2018.11.041.

[18] J. Nie, Y. Xu, L. Zhang, S. Fan, F. Xu, L. Cheng, J. Ma, X. Yin, Microstructure, thermophysical, and ablative performances of a 3D needled C/C-SiC composite, International Journal of Applied Ceramic Technology. 7 (2010) 197–206. doi:10.1111/j.1744-7402.2008.02341.x.

[19] J. Schulte-Fischedick, A. Zern, J. Mayer, M. Rühle, M. Frieß, W. Krenkel, R. Kochendörfer, The morphology of silicon carbide in C/C-SiC composites, Materials Science and Engineering A. 332 (2002) 146–152. doi:10.1016/S0921-5093(01)01719-1.

[20] R. Pampuch, J. Bia, E. Walasek, Mechanism of Reactions in the Si + Cf System and the Self-Propagating High-Temperature Synthesis of Silicon Carbide, Ceramics International. 13 (1987) 63–68.

[21] O.J. Ilegbusi, J. Yang, M.D. Mat, D. Lewis, E.S. Oran, A mesoscopic scale analysis of the reaction-bonded SiC process, Composites Part A. 30 (1999) 339–348.

[22] P. Sangsuwan, A. Orejas, J.E. Gatica, S.N. Tewari, M. Singh, Reaction-Bonded Silicon Carbide by Reactive Infiltration, Industrial & Engineering Chemistry Research. (2001) 5191–5198. doi:10.1021/ie001029e.

[23] Y. Chiang, R.P. Messner, C.D. Terwilliger, Reaction-formed silicon carbide, Materials Science and Engineering A. 144 (1991) 63–74.

7 Figure Captions

Figure 1: Carbon-Carbon (C/C) preform after CVI and before silicon infiltration: (a) Schematic arrangement of non-woven fiber cloth, short cut web and needle stitches; (b) C/C preform (SEM cross-section); (c) non-woven cloth fiber bundle (SEM cross-section); (d) fibers in the short-cut web (SEM cross-section).

Figure 2: XRD analyses of C/C-SiC composites fabricated by (a) GSI and (b) GSI+LSI.

Figure 3: C/C-SiC composites fabricated by GSI with different reaction times (SEM cross-sections): (a) 0.5 h; (b) 1.0 h; (c) 1.5 h; (d) 2.0 h. Magnified images from the inset boxes are shown in (e) to (h).

Figure 4: C/C-SiC composites fabricated by GSI with different reaction times (high magnification SEM cross-sections; 0.5 h (a) & (e); 1.0 h (b) & (f); 1.5 h (c) & (g); 2.0 h (d) & (h). Images (b), (e), and (f) are obtained in backscatter electron mode, the others by secondary electron imaging.

Figure 5: C/C-SiC composites fabricated by GSI+LSI with different GSI reaction times (SEM cross-sections): (a) 0.5 h; (b) 1.0 h; (c) 1.5 h; (d) 2.0 h.

Figure 6: EDS analyses of C/C-SiC composites fabricated by GSI with different reaction times: (a) 0.5 h; (b) 1.5 h; (c) 2.0 h. Fibers in (a) and (c) are from the web region.

Figure 7: SiC morphologies of C/C-SiC composites fabricated by GSI with different reaction time (SEM secondary electron imaging): 0.5 h (a) & (e); 1.0 h (b) & (f); 1.5 h (c) & (g); 2.0 h (d) & (h). The corresponding GSI+LSI composites are shown in: (i) 0.5 h GSI + 2 h LSI; (j) 1.0 h GSI + 2 h LSI; (k) 1.5 h GSI + 2 h LSI; (l) 2.0 h GSI + 2 h LSI. .

Figure 8: 3D visualizations of SiC morphology (labelled XCT, after etching) of C/C-SiC composites: (a) 1.0 h GSI only; (b) 2.0 h GSI only; (c) 1.0 h GSI +2.0 h LSI.

Figure 9: 3D visualizations of porosity (labelled XCT, no etching) of C/C-SiC composites: (a) 1.0 h GSI only; (b) 2.0 h GSI only; (c) 1.0 h GSI +2.0 h LSI.

Figure 10: Open pore distributions in C/C-SiC composites (MIP): (a) GSI; (b) GSI+LSI.

Figure 11: Typical load-displacement curves in flexural tests of C/C-SiC composites: (a) GSI; (b) GSI+LSI.

Figure 12: Fractography (SEM) of C/C-SiC composites fabricated by (a) GSI and (b) GSI+LSI with different GSI reaction times: (i) 0.5 h; (ii) 1.0 h; (iii) 1.5 h; (iv) 2.0 h.

Figure 13: XCT after fracture testing of C/C-SiC composites: (a) 1.0 h GSI and (b) 2.0 h GSI. 3D visualizations of the cracks in the 2.0 h GSI sample are shown in (c).

Table 1 Density and phase composition of C/C-SiC composites fabricated by GSI. Average values ± sample standard deviation (n=3).

Reaction temperature (℃)	Reaction time (h)	C/C-SiC density (g/cm^3)	C content (Vol%)	SiC content (Vol%)	Si content (Vol%)	Porosity (Vol%)	Porosity by MIP (Vol%)
1700	0.5	1.29 ±0.11	68.65 ±0.18	1.02 ±0.11	0.42 ±0.02	29.91 ±0.09	27.5
	1.0	1.70 ±0.09	66.45 ±0.41	14.65 ±0.05	0.52 ±0.09	18.38 ±0.43	16.9
	1.5	1.95 ±0.06	59.06 ±0.44	24.78 ±0.18	3.63 ±0.03	12.52 ±0.25	8.9
	2.0	2.08 ±0.07	56.23 ±0.20	25.35 ±0.22	12.03 ±0.90	6.39 ±0.80	2.6

Table 2 Density and phase composition of C/C-SiC composites fabricated by GSI + LSI. Average values ± sample standard deviation (n=3).

Reaction temperature (℃)	Reaction time (h)		C/C-SiC density (g/cm^3)	C content (Vol%)	SiC content (Vol%)	Si content (Vol%)	Porosity (Vol%)	Porosity by MIP (Vol%)
	GSI	LSI						
1700	0.5	2	2.17 ±0.03	53.64 ±0.19	25.62 ±0.18	15.83 ±0.15	4.91 ±0.15	4.6
	1.0		2.25 ±0.03	56.10 ±1.01	29.83 ±0.64	11.32 ±0.24	2.75 ±0.29	2.0
	1.5		2.19 ±0.04	56.09 ±1.47	27.15 ±0.77	12.42 ±0.59	4.34 ±0.34	2.2
	2.0		2.11 ±0.06	53.37 ±0.55	26.24 ±0.72	14.87 ±0.81	5.52 ±0.64	1.8

Table 3 Flexural strength and modulus of C/C-SiC composites. Average values ± standard deviation (n=5).

Reaction time (h)	GSI		GSI+LSI	
	Flexural strength (MPa)	Modulus (GPa)	Flexural strength (MPa)	Modulus (GPa)
0.5	116.8±17.8	14.3±2.6	202.8±7.8	27.6±2.1
1.0	138.7±8.0	18.6±4.1	204.3±7.5	31.7±3.2
1.5	151.0±17.9	22.3±3.8	173.6±9.4	31.5±3.3
2.0	185.4±16.7	25.8±5.8	145.6±15.7	28.3±4.3

Figure 1

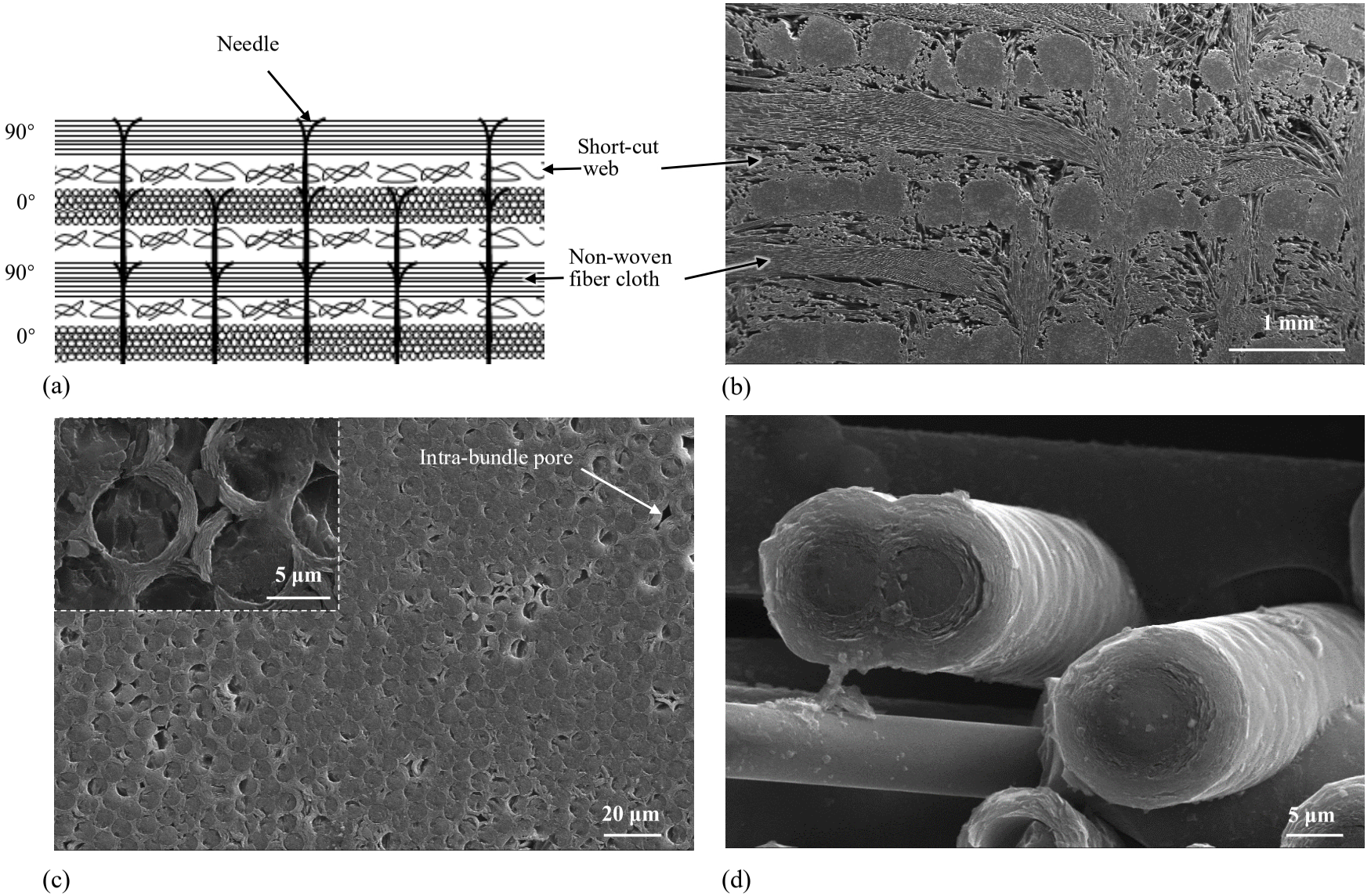
Needle
90°
0°
90°
0°
Short-cut web
Non-woven fiber cloth
(a)
1 mm
(b)
Intra-bundle pore
5 μm
20 μm
(c)
5 μm
(d)

Figure 2

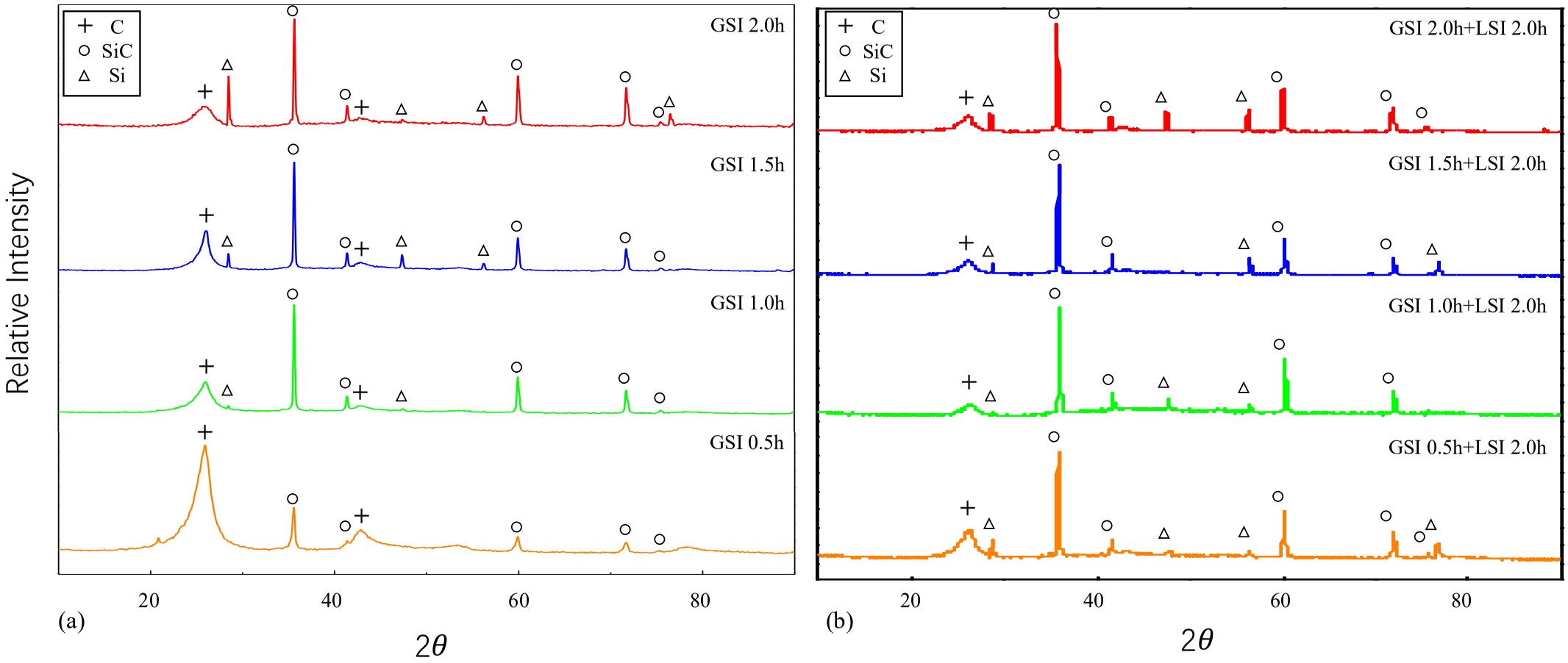
C
SiC
Si
GSI 2.0h
GSI 1.5h
GSI 1.0h
GSI 0.5h
Relative Intensity
20
40
60
80
(a)
2θ
GSI 2.0h+LSI 2.0h
GSI 1.5h+LSI 2.0h
GSI 1.0h+LSI 2.0h
GSI 0.5h+LSI 2.0h
(b)

Figure 3

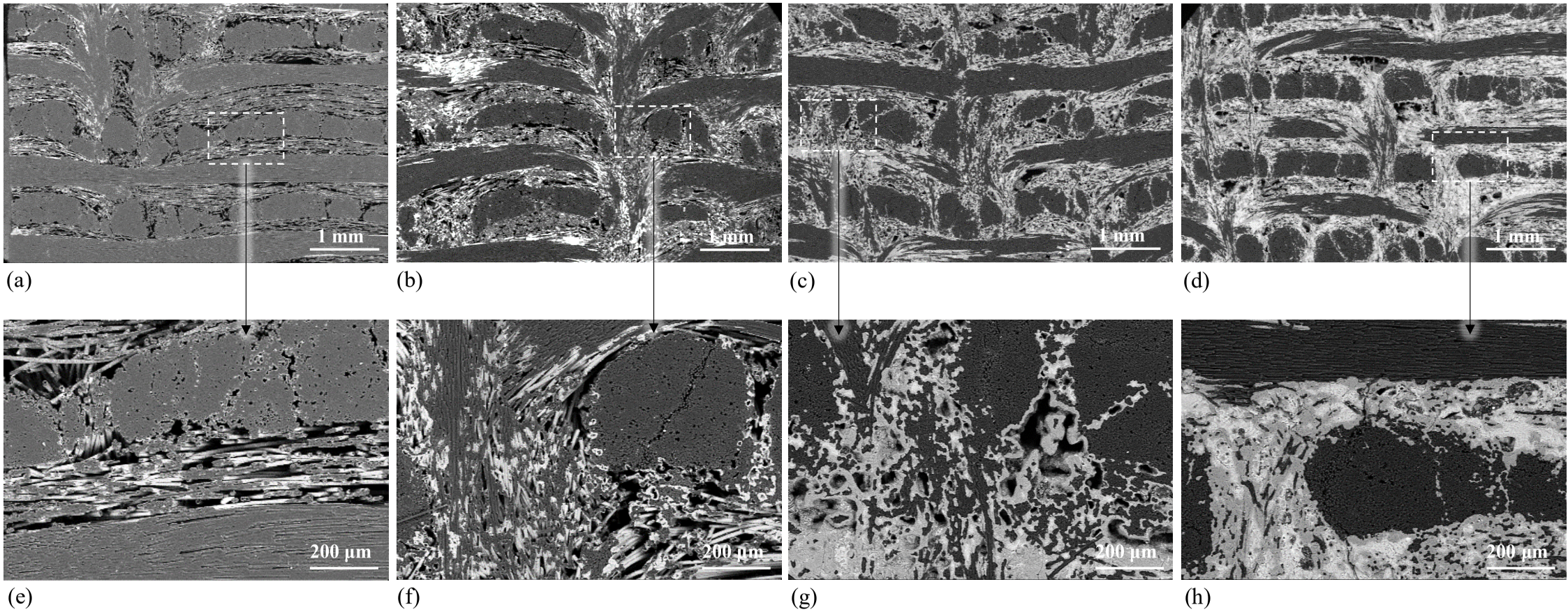

Figure 4

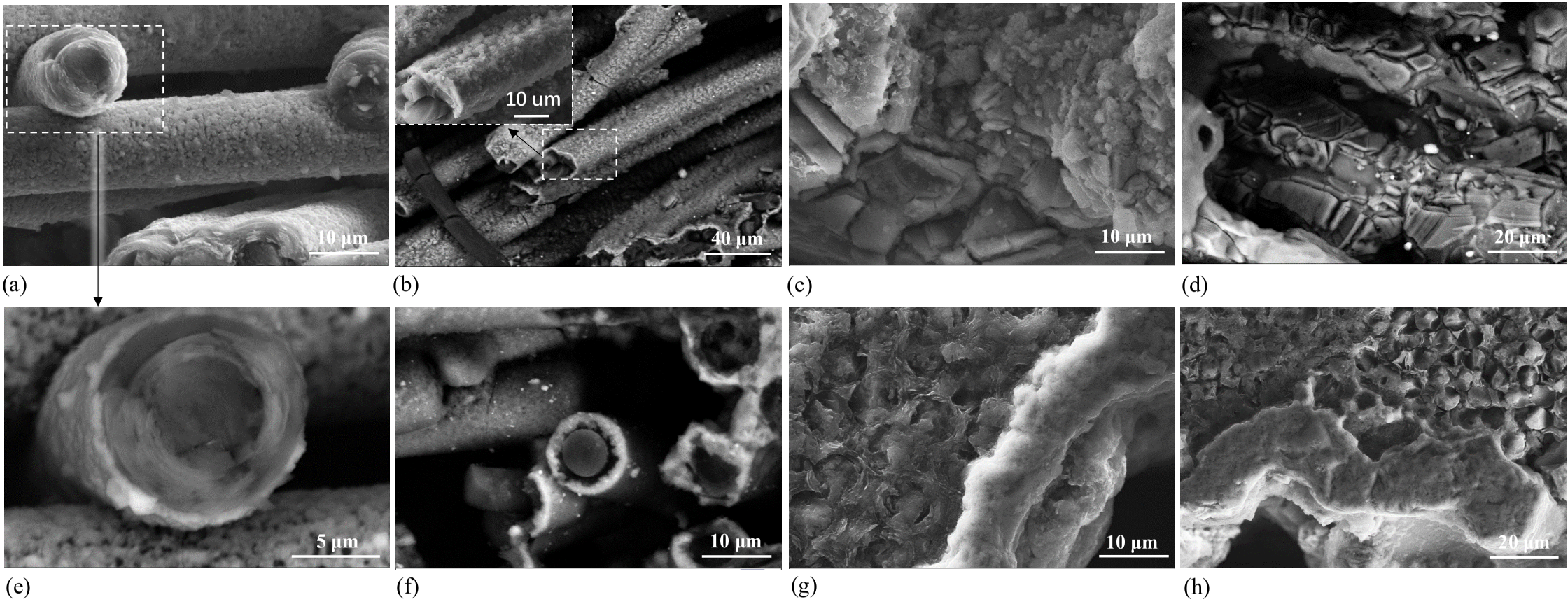

Figure 5

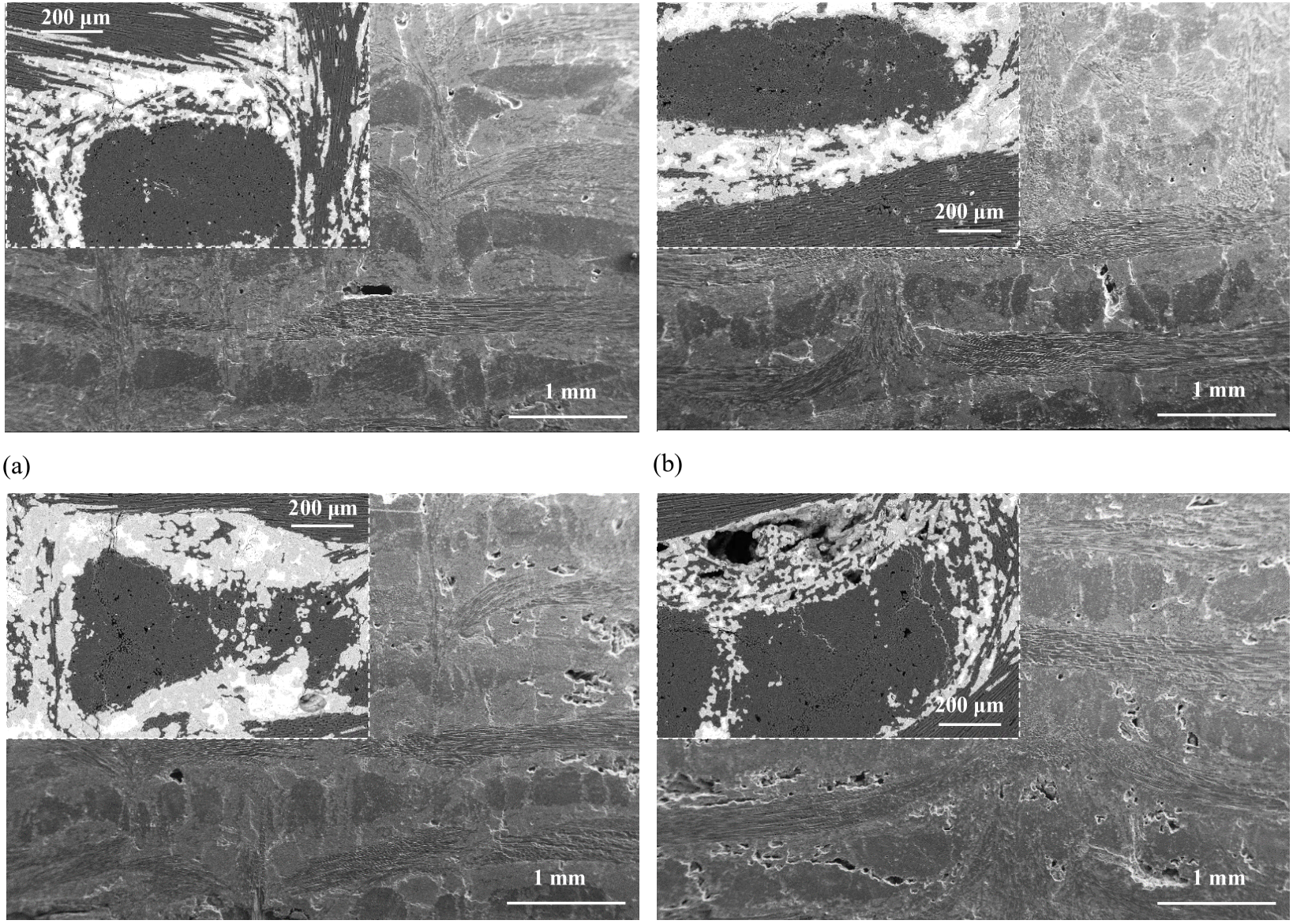

Figure 6

(a)

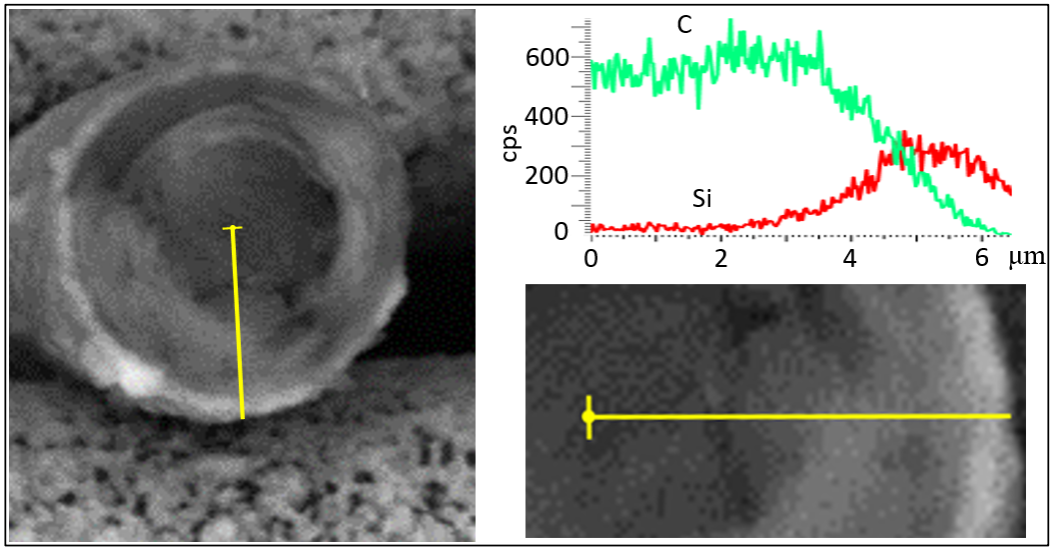

(c)

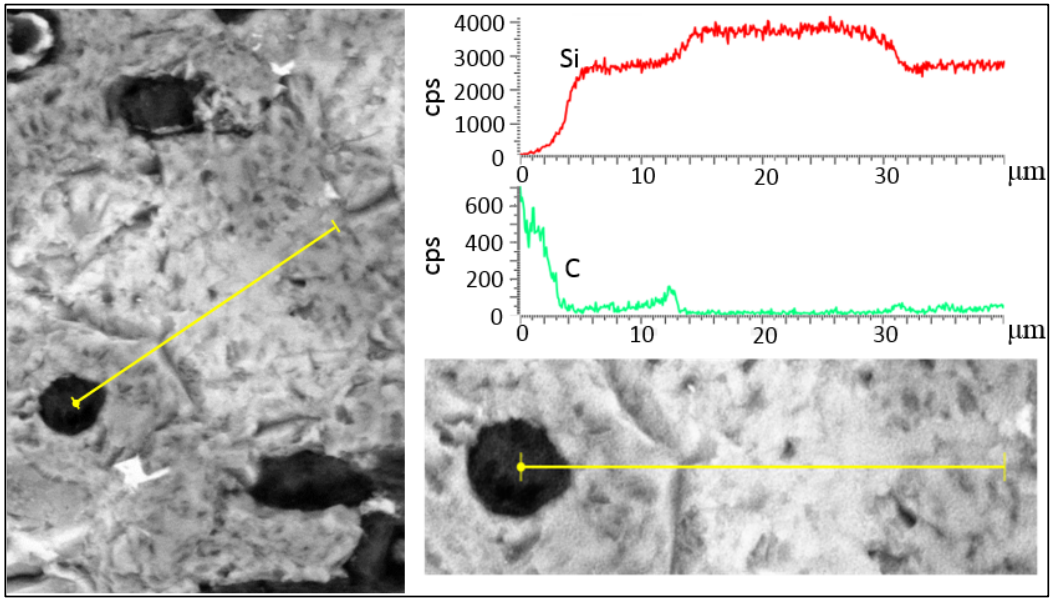

(b)

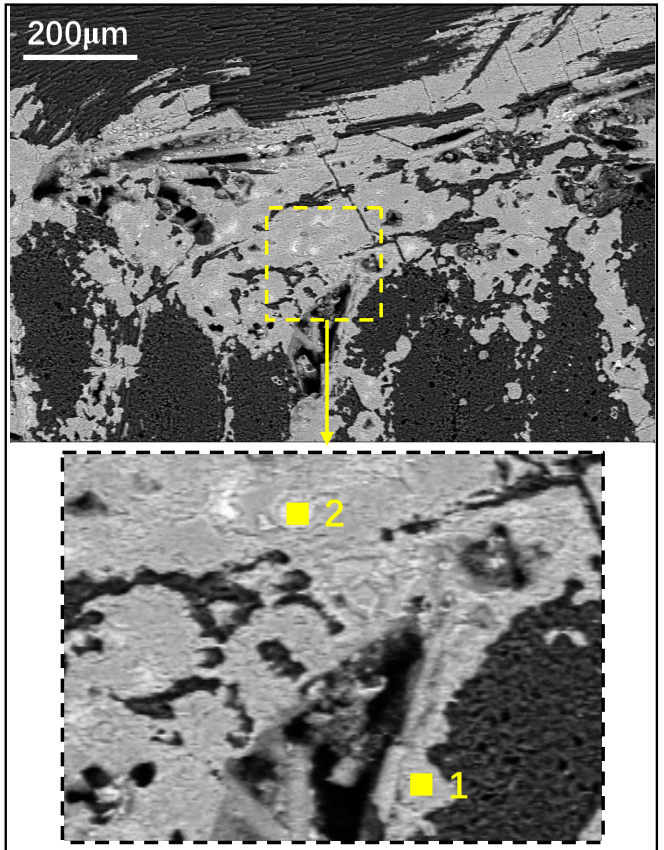

Point	Element	Atomic percentage (%)	Elemental mass ratio (%)
1	C	54.93	34.26
	Si	45.07	65.74
2	C	22.47	11.03
	Si	77.53	88.97

Figure 7

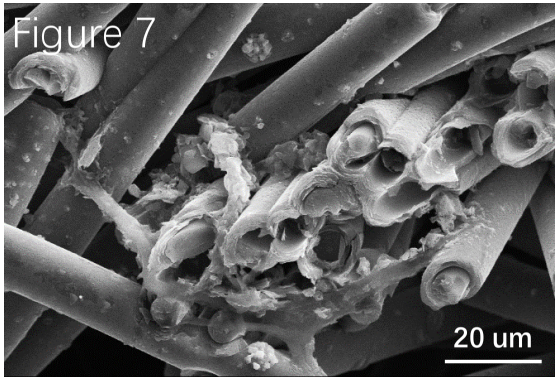

(a)

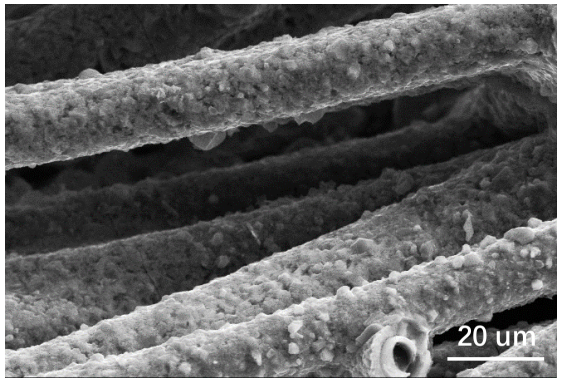

(b)

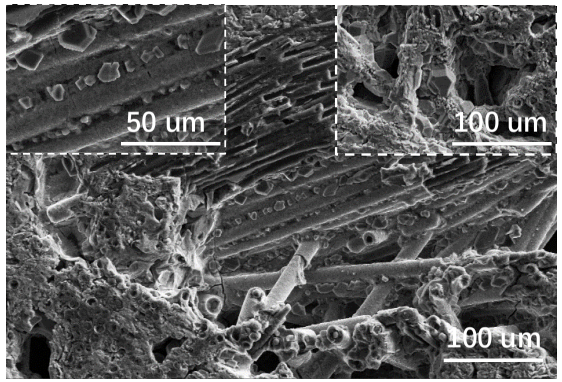

(c)

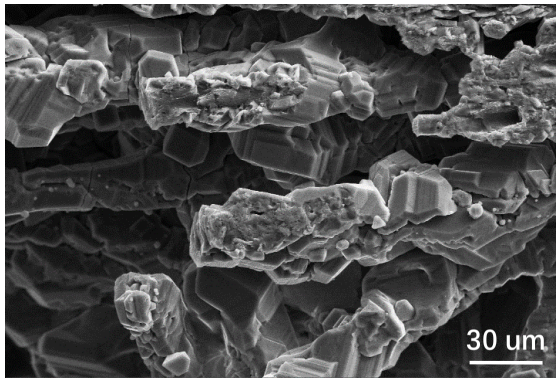

(d)

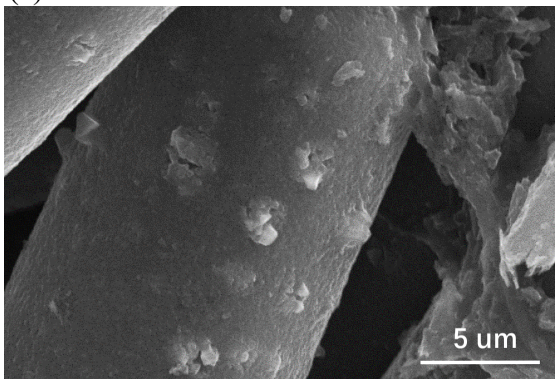

(e)

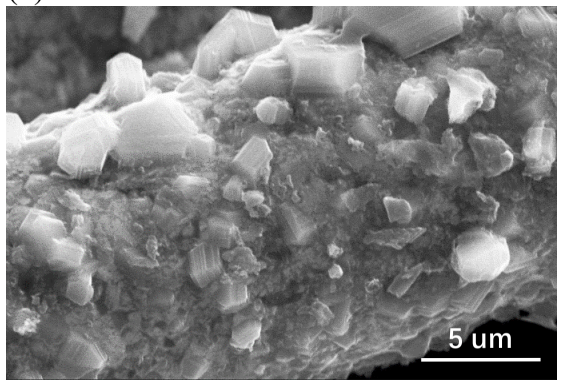

(f)

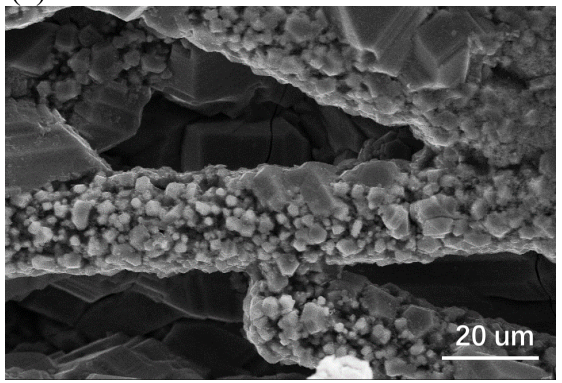

(g)

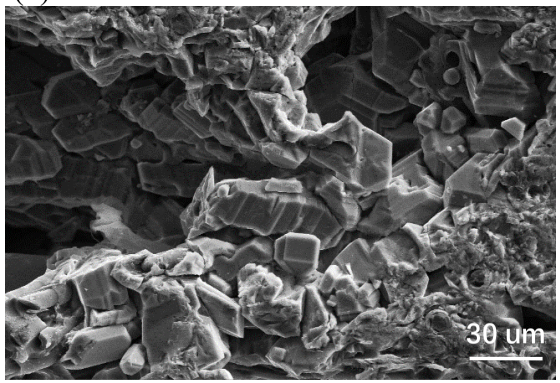

(h)

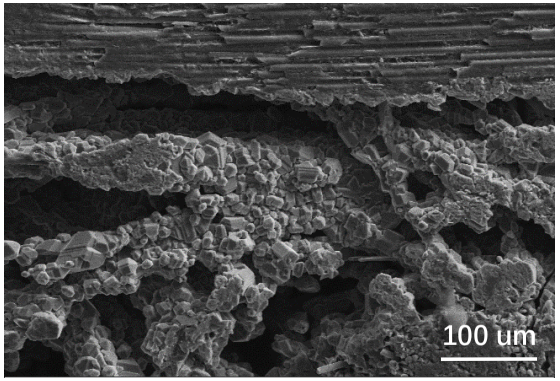

(i)

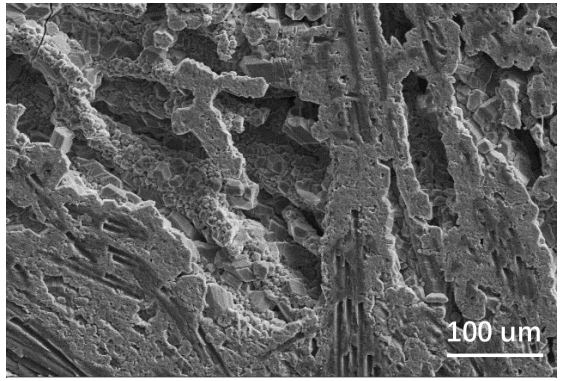

(j)

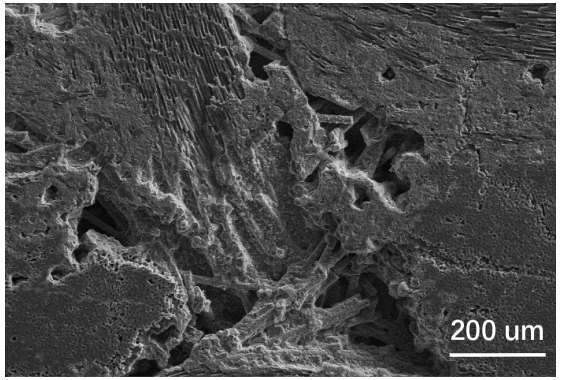

(k)

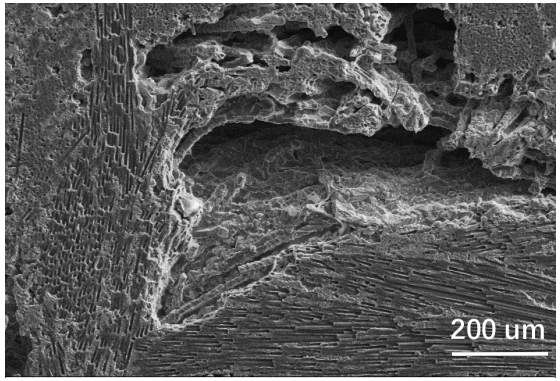

(l)

Figure 8

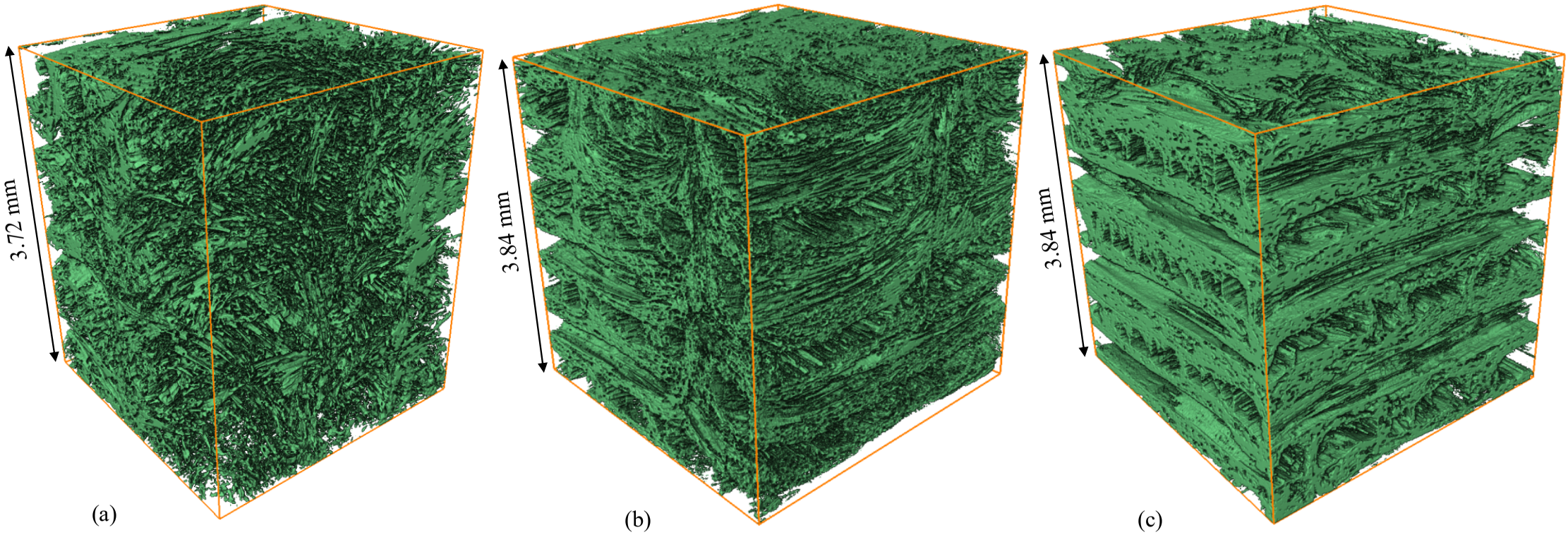

Figure 9

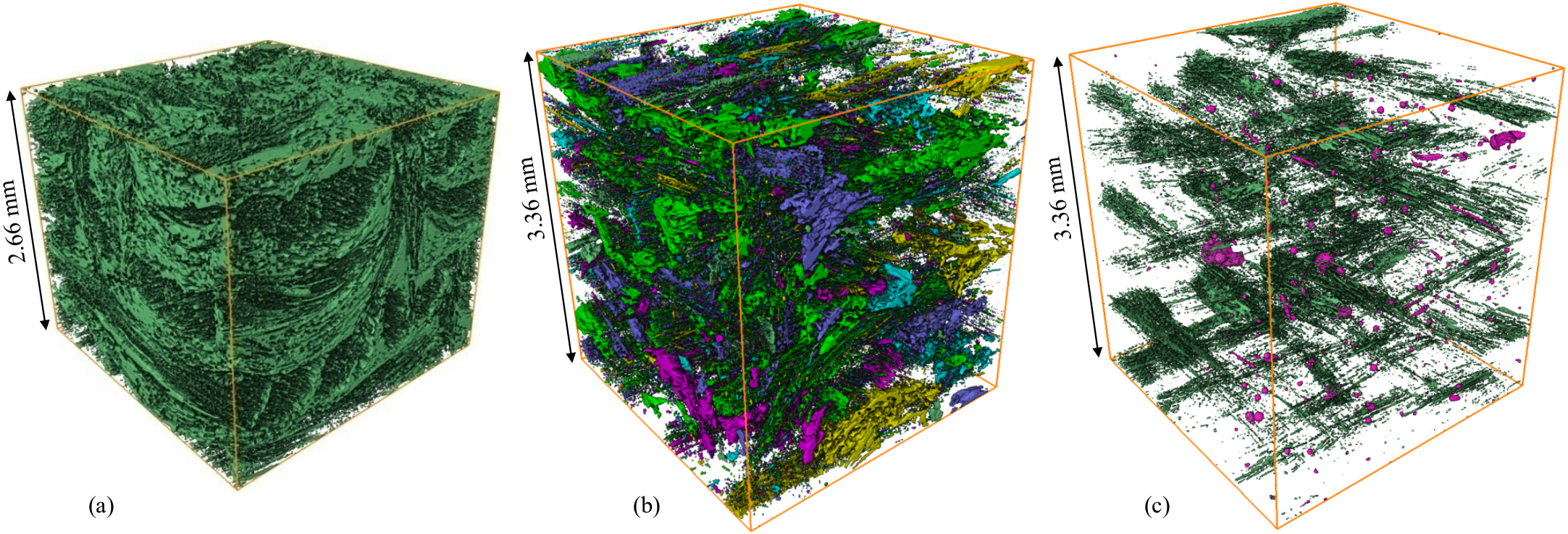

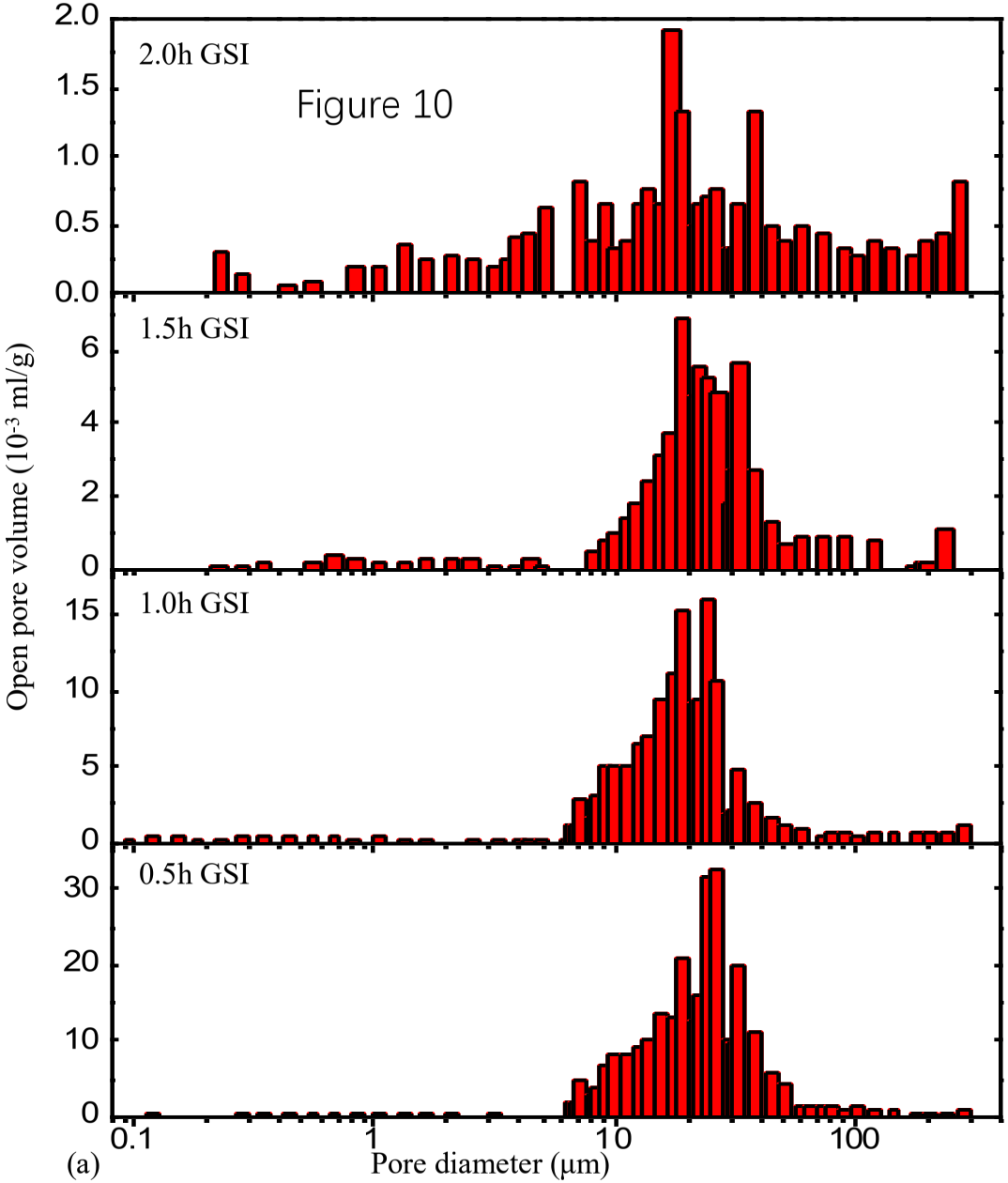
2.0h GSI
Figure 10
1.5h GSI
1.0h GSI
0.5h GSI
Open pore volume (10-3 ml/g)
Pore diameter (μm)
(a)

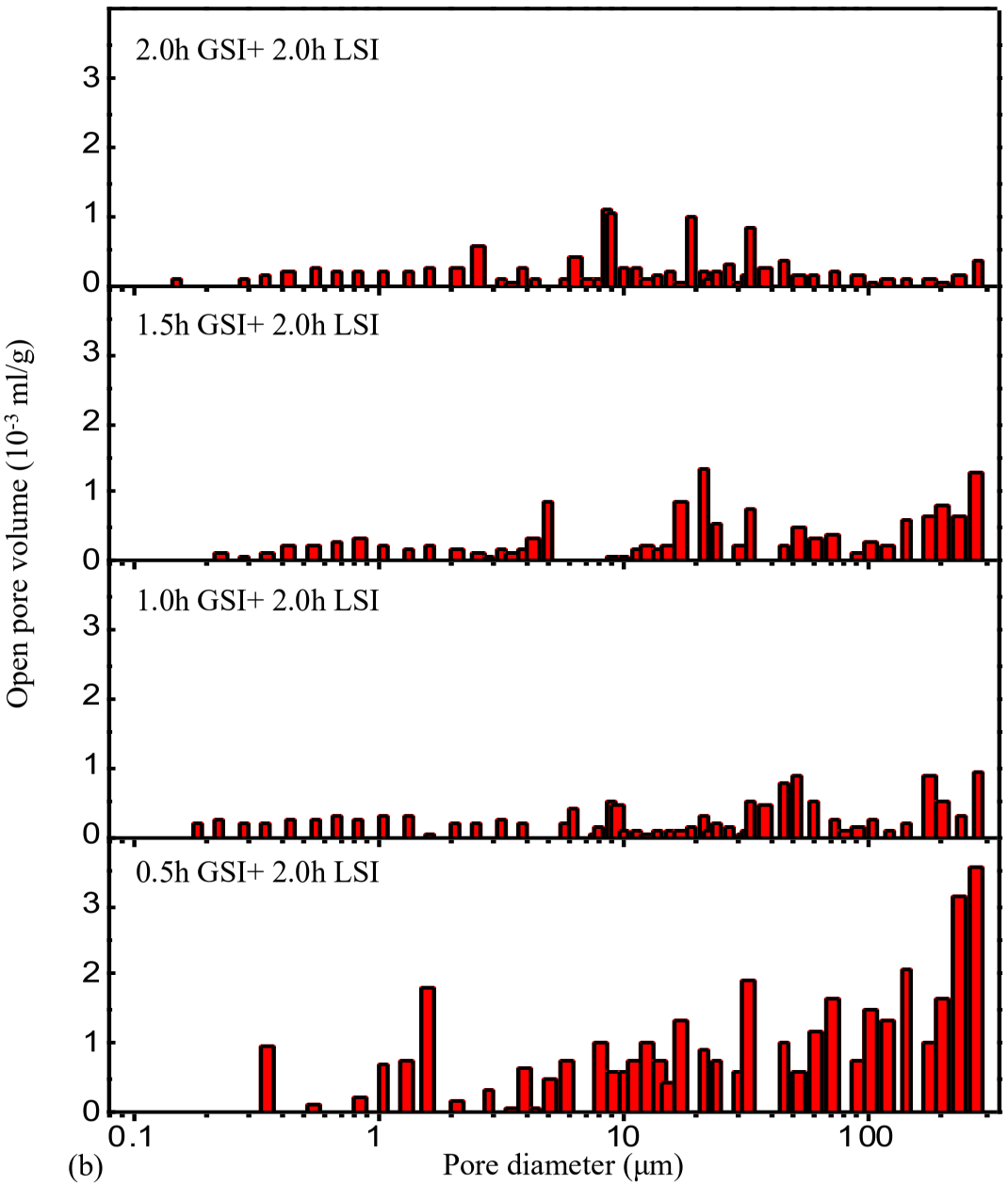
2.0h GSI+ 2.0h LSI
1.5h GSI+ 2.0h LSI
1.0h GSI+ 2.0h LSI
0.5h GSI+ 2.0h LSI
Open pore volume (10-3 ml/g)
Pore diameter (μm)
(b)

Figure 11

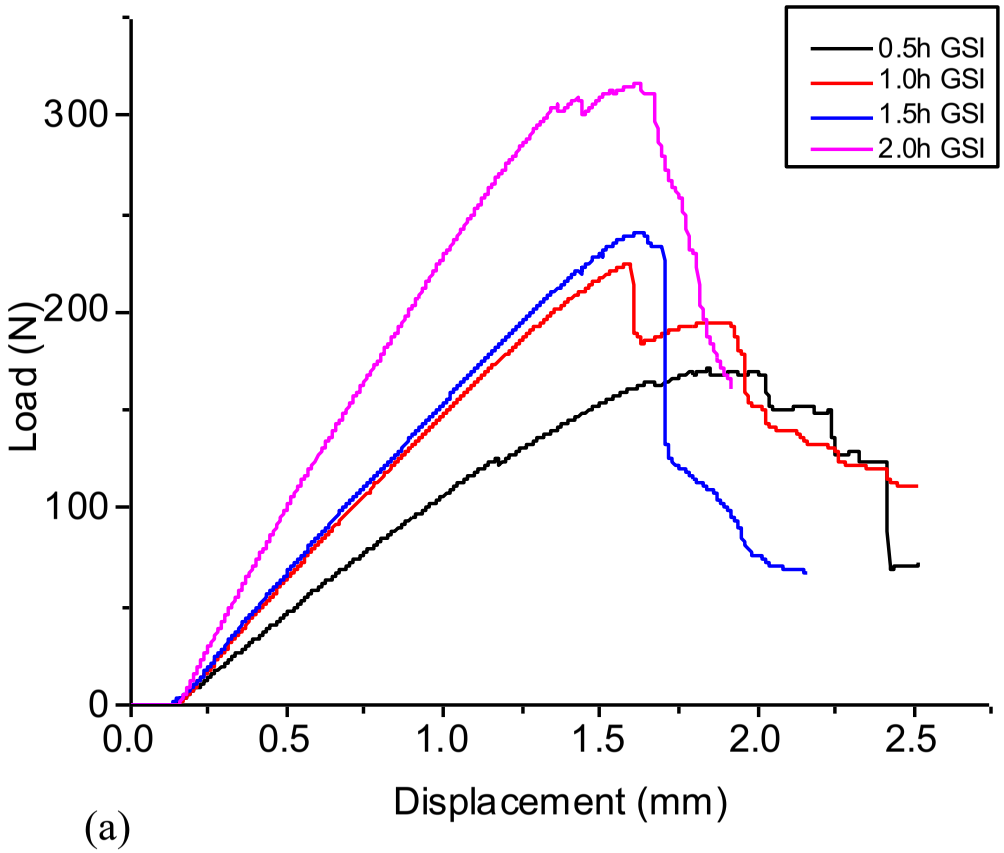
0.5h GSI
1.0h GSI
1.5h GSI
2.0h GSI
Load (N)
Displacement (mm)
0
100
200
300
0.0
0.5
1.0
1.5
2.0
2.5

(a)

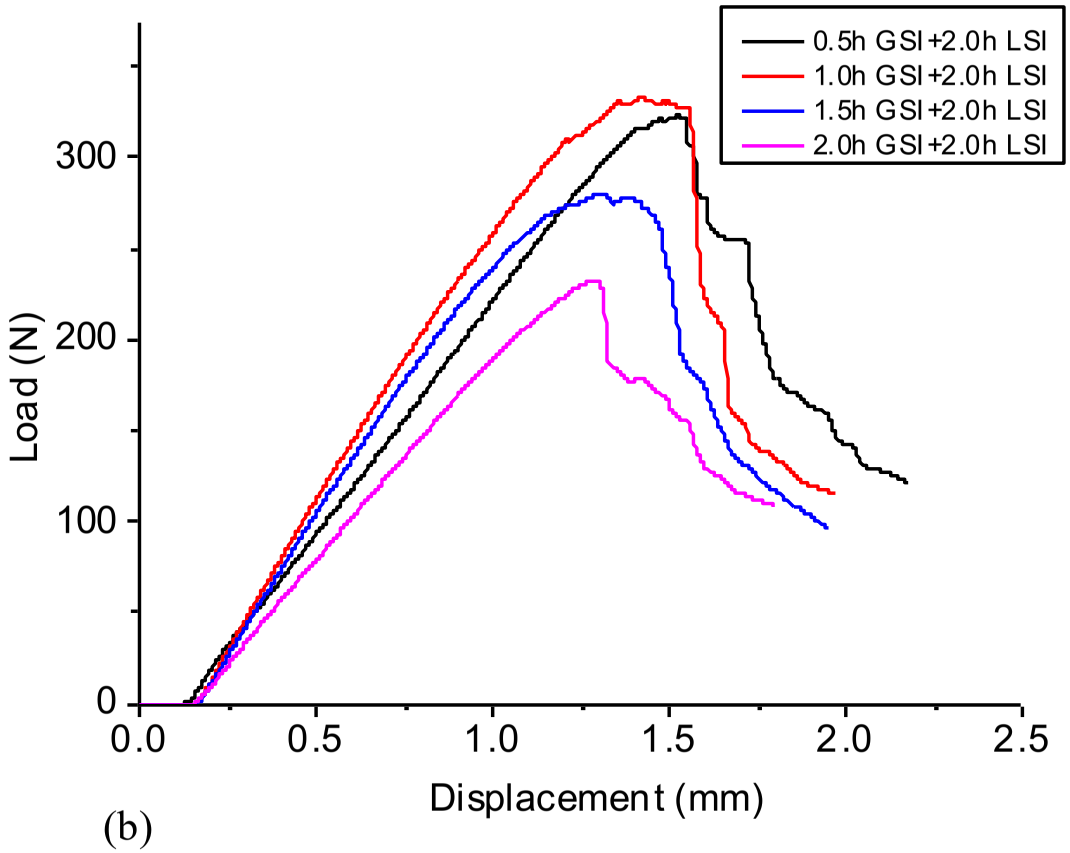
0.5h GSI+2.0h LSI
1.0h GSI+2.0h LSI
1.5h GSI+2.0h LSI
2.0h GSI+2.0h LSI
Load (N)
Displacement (mm)
0
100
200
300
0.0
0.5
1.0
1.5
2.0
2.5

(b)

Figure 12

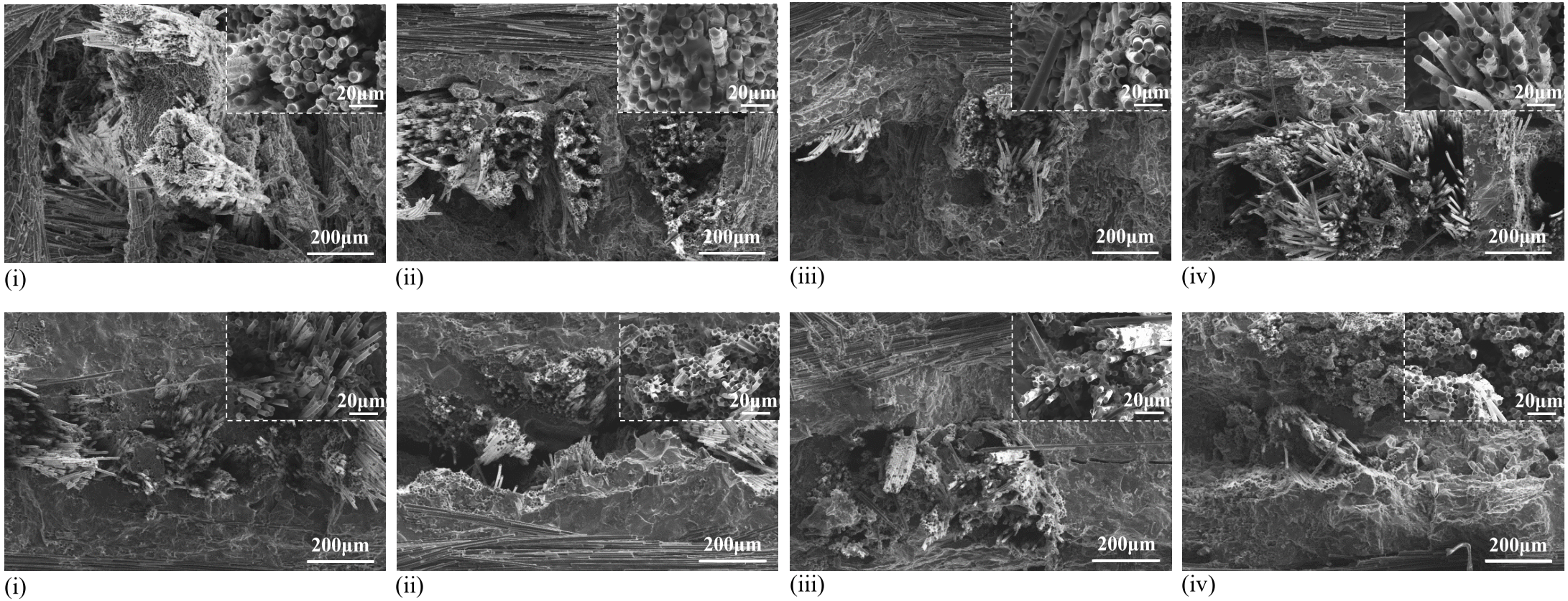

Figure 13

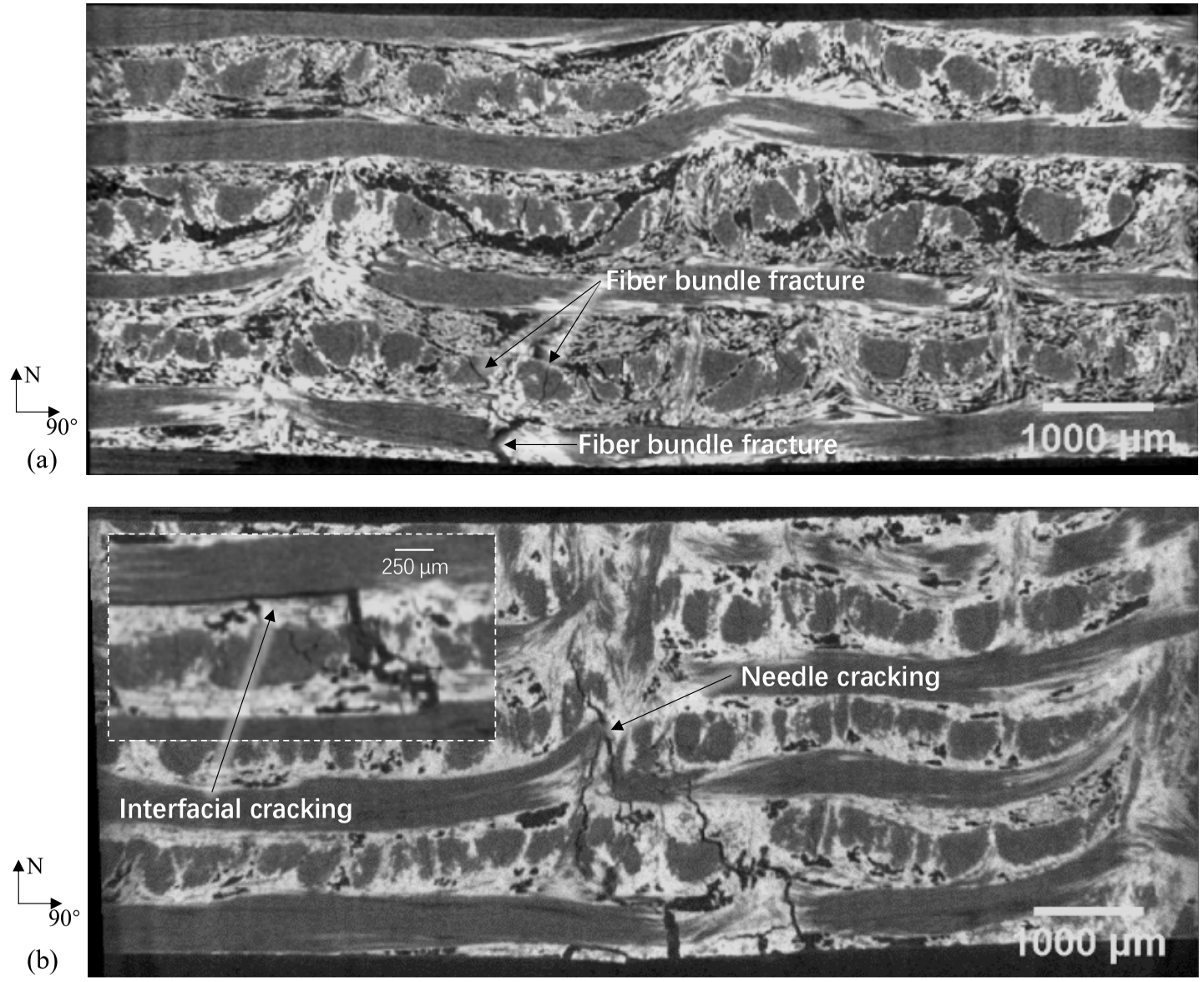
Fiber bundle fracture
Fiber bundle fracture
1000 μm
N
90°
(a)
250 μm
Needle cracking
Interfacial cracking
1000 μm
N
90°
(b)

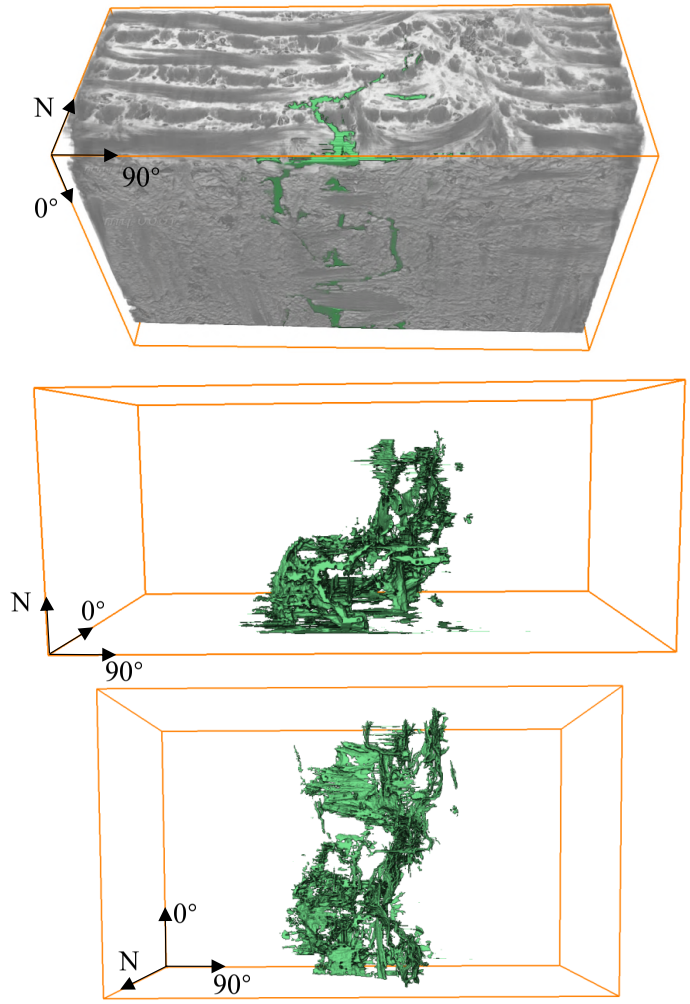
N
90°
0°
N
0°
90°
0°
N
90°
(c)